PHYSICS OF FLUIDS **17**, 116601 (2005)

Steady rotating flows over a ridge

J. G. Esler,[a] O. J. Rump, and E. R. Johnson
Department of Mathematics, University College London, 25 Gower Street, London WC1E 6BT, United Kingdom

(Received 6 June 2005; accepted 4 October 2005; published online 11 November 2005)

A model describing rotating single-layer flows over a parabolic ridge is investigated. A method of constructing steady solutions is introduced, and is used to extend previous results and determine exact regime diagrams describing the qualitative nature of the solution. Analytic expressions for the boundaries between transcritical flow and supercritical and subcritical flows are given as a function of obstacle height, Froude number of the upstream flow, and the flow inverse Burger number (a nondimensional number proportional to the square of the rotation rate). For fixed obstacle height, the nature of the supercritical transition is found to change as the rotation rate increases, with a hysteresis region like that in nonrotating flow being present only at lower rotation rates. At higher rotation rates, solutions with stationary jumps over the obstacle become stable, and abrupt transitions between supercritical and transcritical flow no longer occur. An exact analytic expression is also found for transcritical flow over the obstacle, which is closely related to the solutions for nonlinear inertia-gravity waves of limiting amplitude found by Shrira. For sufficiently high ridges in initially supercritical flow, a wave train of nonlinear inertia-gravity waves of limiting amplitude appears behind a downstream hydraulic jump. © *2005 American Institute of Physics*.
[DOI: 10.1063/1.2130740]

I. INTRODUCTION

The shallow water model plays a central role in our understanding of nonrotating flow over topography (see, e.g., the review material in Baines[1]). The model's utility derives from its amenability to analytic solution, its robustness in being fully nonlinear, and the readiness with which nonlinear concepts related to hydraulic control can be explicitly demonstrated. Under conditions where the aspect ratio of the layer flow in question is sufficiently small, the shallow water model can be quantitatively relevant to both oceanic and atmospheric flows.[2] Hydraulic jumps may be included as "weak" solutions of the equations (mass and momentum conserving jumps in surface height and velocity), and it has been argued[3] that these are a reasonably accurate model of the situation at steadily propagating bores, i.e., after initial nonlinear wavebreaking has taken place.

Although linear solutions in rotating flow over topography have a relatively long history,[4,5] solutions involving the direct extension of the full nonlinear equations to rotating flows appear not to have been considered until Sambuco and Whitehead[6] and Baines and Leonard[7] (hereafter referred to as BL). Sambuco and Whitehead give an approximate treatment of the case of transcritical flow over an obstacle, supported by experiments, whereas BL describe a numerical study of the flow over a semi-infinite linear ridge. Both studies found that in the presence of rotation, critical conditions over the obstacle still control the flow, as in the case of nonrotating flow. The point of critical transition, however, need no longer coincide with obstacle crest.[6] BL went on to show that rotation causes upstream propagating bores either to stop at some distance ahead of the obstacle, or, in the case of initially subcritical flow, disappear completely in the steady state. In the case of initially supercritical flow, finite-amplitude inertia-gravity wave trains appeared downstream of the obstacle. Rotation also reduced the size of the region of parameter space allowing transcritical flow over the obstacle.

Unlike nonrotating solutions, rotating solutions necessarily apply only to the case of an infinite ridge without sidewalls, since rotation induces a flow parallel to the ridge. However, the solutions are still one-dimensional as the flow is independent of the along-ridge coordinate. Figure 1 illustrates three possible physical scenarios to which the solutions apply. The first scenario describes "one-and-a-half" layer flow, where a layer of density ρ_2 and finite depth lies underneath a semi-infinite layer of density ρ_1. In the Boussinesq limit $(\rho_2-\rho_1)/\rho \ll 1$, the interface between the two layers remains flat when a constant uniform flow of arbitrary but equal strength is present in each layer. A one-and-a-half layer flow of this type is a useful physical model for commonly occurring atmospheric flows, where the lower layer may be taken to be the marine boundary layer, with depth around 1 km, and the upper layer the free troposphere above. The second scenario illustrated is that of oncoming flow in a single layer. For the solutions presented herein to remain relevant in this case, the flow must be subject to an imposed pressure gradient in the along-ridge direction. If the imposed pressure gradient is absent, the free surface will tilt in the along-ridge direction to balance the Coriolis force on the flow, which is a further complicating feature of rotating channel flows. However, BL's solutions have also been discussed in the single-layer oceanic context[8] as a useful paradigm for understanding aspects of rotating hydraulic flow in

---

[a] Author to whom correspondence should be addressed. Electronic mail: gavin@math.ucl.ac.uk

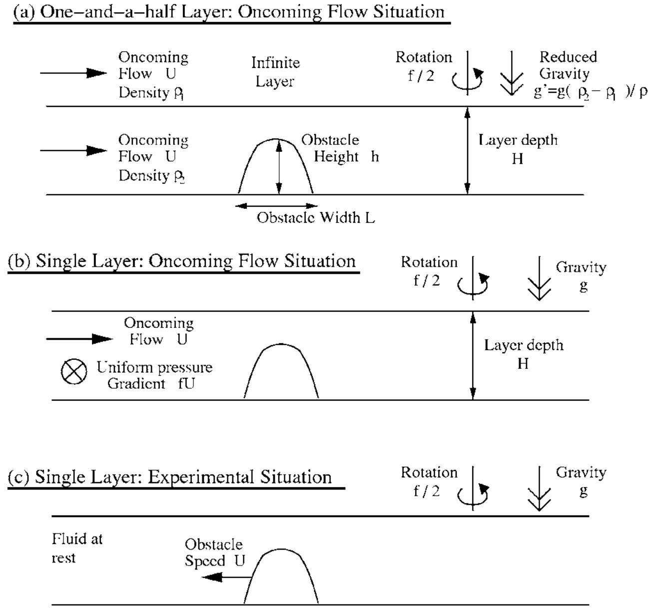

FIG. 1. Schematic showing the three physical scenarios described in the text.

a channel, in order to help quantify sidewall effects (e.g., due to Kelvin waves).

The third scenario for which the solutions are relevant is the "experimental scenario" where the obstacle is accelerated into an initially undisturbed fluid. In this case, no imposed pressure gradient is necessary. The interpretation of towing-tank experimental studies such as those of Maxworthy[9] and more recently Johnson *et al.*[10] may be facilitated by the solutions presented in BL and in this paper, although dispersive effects remain important in the parameter regimes of the experiments. Recent analytical and numerical work, corresponding to the experimental scenario, by Vilenski and Johnson[11] has highlighted rich behavior involving multiple solitary wave generation ahead of and behind the obstacle in single-layer flow in the two-dimensional Ostrovsky (or rotating Kadomtsev-Petviashvili) equations.[12–14] Baines[15] also makes the point that the experimental scenario shown in Fig. 1 is relevant to the atmospheric situation of an advancing cold front, where the cold air mass is treated as the advancing obstacle.

One point of particular interest in all of the above scenarios concerns the presence or absence of a downstream jump followed by the generation of wave trains of inertia-gravity waves downstream of the obstacle. It is well known[16,17] that inertia-gravity waves of finite amplitude exist in the rotating shallow water system. These waves are known to have a maximum limiting amplitude, and at this amplitude the waves have broad troughs and sharply pointed crests, with a finite jump in wave slope at each crest. However, little is known about the generation by topography of these waves. For example, BL did note the existence of downstream jumps and wave trains but did not highlight the conditions under which they are generated. A deeper understanding of the generation of downstream jumps and waves may allow interpretation of the apparently climatic nonlinear flow patterns around islands such as Guadalupe, Baja California, and St. Lawrence Island in the Bering Sea as illustrated by photographs of cloud distributions and synthetic aperture radar.[10,18,19]

This paper extends the discussion of BL by presenting exact solutions for the specific case of flow over a parabolic ridge, with the aim of developing understanding of this important paradigm of rotating flow over topography. In Sec. II, the steady flow equations to be solved are derived from the shallow water equations. The behavior at the obstacle boundary and at stationary hydraulic jumps is highlighted, and the regime diagram for nonrotating flow is briefly reviewed. In Sec. III, a method of construction of steady solutions of the rotating equations is introduced, and used to determine exact regime diagrams for the solutions in the rotating case. A connection with the limiting amplitude inertia-gravity wave-train solutions of Shrira[16,17] is highlighted and exploited to obtain exact analytic expressions for transcritical flow over the obstacle. In Sec. IV, numerical solutions using a finite-volume numerical scheme are used to verify the semianalytic solutions, and explore the behavior in the regions of hysteresis identified analytically. Section V discusses the results.

II. MODEL EQUATIONS AND BACKGROUND

A. Rotating one-dimensional shallow water equations

Consider the experimental scenario, shown in Fig. 1(c), of a one-dimensional obstacle of height h and width L advancing at speed U into a fluid of depth H, rotating at rate $f/2$ and under gravity g, which is initially at rest. The nondimensional shallow water equations in the frame of the obstacle are

$$\begin{aligned} &u_t + uu_x - \sqrt{B}v = -\sigma_x - Mb_x, \\ &v_t + uv_x + \sqrt{B}(u-F) = 0, \qquad (1) \\ &\sigma_t + (u\sigma)_x = 0. \end{aligned}$$

Here, the layer depth σ is scaled on H, the velocity components in the frame of the obstacle (u,v) are scaled on the gravity wave speed $c=\sqrt{gH}$, the obstacle elevation b is scaled on h, length x is scaled on L, and time t on L/c. The nondimensional parameters in Eq. (2) are

$$F = \frac{U}{c}, \quad M = \frac{h}{H}, \quad B = \frac{f^2L^2}{c^2} = \frac{f^2L^2}{gH}.$$

These may be interpreted as a Froude number F of the relative flow, a nondimensional obstacle height M, and an inverse Burger number B, the square of the ratio of the obstacle scale to the radius of deformation (note that B is related to BL's obstacle length A via $B=A^2$). Additionally, the upstream conditions to be satisfied are $\sigma \to 1$, $u \to F$ as $x \to -\infty$.

If the resulting flow is assumed steady, and solutions are sought that are purely a function of x, the thickness equation may be integrated to give $u\sigma = F$, allowing u and subsequently v to be eliminated from (1) to give a single equation,[20]

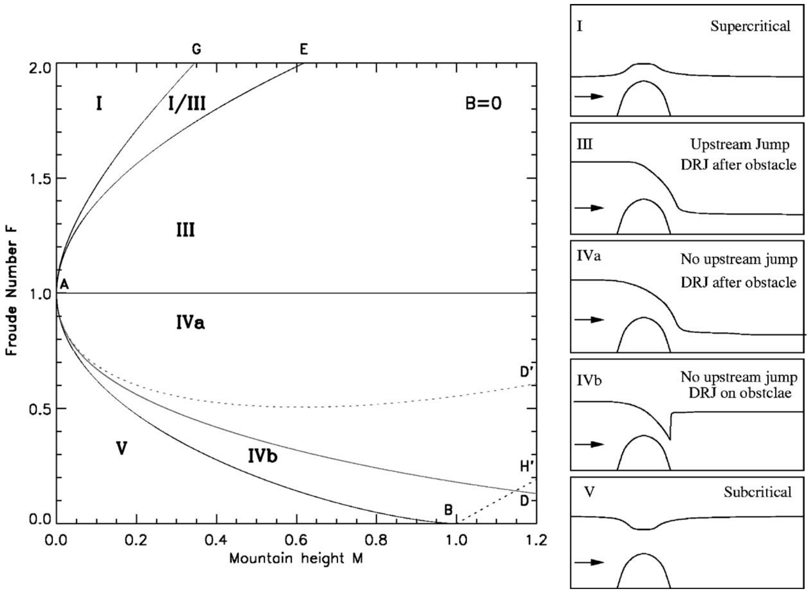

FIG. 2. An obstacle height/Froude number (M,F) regime diagram for steady (and quasisteady) solutions in the nonrotating case, following Lawrence (Refs. 22 and 23) and Baines (Ref. 1). Solid curves mark the boundaries between steady regimes for the rotating solutions described in Sec. III in the limit of weak rotation $B \to 0$. Dotted curves mark the boundaries between quasisteady regimes in the nonrotating case $B=0$ (see text). The steady regimes are as follows: (I) Supercritical flow everywhere. (III) Transcritical flow over the obstacle with an upstream jump. (IVa) Transcritical flow over the obstacle with no upstream jump and a downstream recovery jump (DRJ) after the obstacle. (IVb) Transcritical flow over the obstacle with no upstream jump and a DRJ on the obstacle. (V) Subcritical flow everywhere. The region I/III is a hysteresis region where more than one solution is possible.

$$\left(\sigma+\frac{F^2}{2\sigma^2}\right)_{xx}+B(1-\sigma)=-Mb_{xx}. \tag{2}$$

Note that u and v are related to σ by

$$u=\frac{F}{\sigma},\quad v=\frac{1}{\sqrt{B}}\left[b_x+\sigma_x\left(1-\frac{F^2}{\sigma^3}\right)\right].$$

As a parabolic obstacle is considered below, it is necessary to consider the situation at points where the obstacle gradient b_x is discontinuous (e.g., at the edges of the parabola). Integrating (2) across such a discontinuity at $x=x_e$ gives

$$\left(1-\frac{F^2}{\sigma^3}\right)[\sigma_x]_-^+=-[b_x]_-^+\quad \text{at } x=x_e. \tag{3}$$

B. Stationary hydraulic jump solutions

BL,[7] following Houghton,[21] argue that because a hydraulic jump may be considered to take place across a very short distance compared to the Rossby radius of deformation ($L_R=c/f$), rotation may be considered to have a negligible effect on its internal dynamics. Hence, across a stationary jump, mass and momentum are conserved. Conservation of mass is implicit in the derivation of (2), as the mass flux is assumed equal to its upstream value everywhere in the steady solution. Conservation of momentum gives

$$\left[\frac{\sigma^2}{2}+\frac{F^2}{\sigma}\right]_-^+=0, \tag{4}$$

which can be rearranged as

$$\sigma_+=\frac{\sigma_-}{2}\left(\left[\frac{8F^2}{\sigma_-^3}+1\right]^{1/2}-1\right). \tag{5}$$

Continuity of v across the jump follows from the original equations (1), and this ensures that

$$\left[\sigma_x\left(1-\frac{F^2}{\sigma^3}\right)\right]_-^+=0. \tag{6}$$

Stationary jumps may therefore appear anywhere in the solutions provided both (5) and (6) are satisfied.

C. One-dimensional flow over an obstacle in the limit of weak rotation

Figure 2 gives the relevant regime diagram for flow behavior in the limit of zero rotation ($B\to 0$) for flow over a two-dimensional obstacle. The regime diagram has much in common with those of Lawrence[22,23] and Baines[1] for nonrotating flows. Lawrence's diagram illustrates the flow regimes that occur when flow controlled by an upstream sluice gate or downstream weir is allowed to become steady over the obstacle. By contrast, the Baines regime diagram describes the steady and quasisteady flows that occur when an obstacle is towed at a constant speed through a fluid initially at rest. Here, a quasisteady solution refers to a solution that includes nonlinear hydraulic jumps propagating outwards to $\pm\infty$. Curves on Fig. 2 represent the boundaries between different types of steady or quasisteady solution. Of the two regime diagrams, Lawrence is more relevant to the rotating solutions described below in the limit of weak rotation ($B\to 0$), and hence our classification of solution regimes I-V closely follows those of Lawrence. Figure 2 and the Lawrence and Baines diagrams share the curves BAE and AG, while a curve in a similar position to AD is present in the Lawrence diagram. The dotted curves AD′ and AH′ which are unique to the Baines diagram are included for completeness.

In region I, the solution is purely supercritical, with the free surface raised over the obstacle, whereas in region V the flow is purely subcritical with the free surface lowered over the obstacle. In region III, the flow is transcritical with a stationary hydraulic jump a large distance ($\gg L$) upstream, and a stationary downstream recovery jump (DRJ) a similarly large distance downstream. In nonrotating flow, in the

Baines scenario, these jumps propagate at constant speed to ±∞, but the presence of even very weak rotation causes them to eventually become arrested. A critical point is located at the obstacle crest where the flow changes from subcritical to supercritical. Region IVa is similar to region III except there is no stationary jump upstream, as the presence of very weak rotation causes the upstream propagating jump present in the nonrotating solution to decay to zero amplitude. In region IVb, there is no stationary upstream jump and the stationary downstream recovery jump is located on the obstacle itself. A brief review of the derivation of the curves in this diagram will be helpful in what follows. The original results are due to Long[24,25] and Houghton and Kasahara,[26] and the hysteresis region (I/III) has been explored in detail by Baines and Davies.[27]

First of all, note that with $B=0$, Eq. (2) can be integrated twice to give

$$\sigma + \frac{F^2}{2\sigma^2} + Mb = K. \tag{7}$$

The condition for this cubic equation to have three real roots at the obstacle summit (where $b=1$) is straightforwardly shown to be

$$K > M + \tfrac{3}{2}F^{2/3}. \tag{8}$$

A symmetric solution such as those in regimes I and V is possible only if $K=1+F^2/2$, i.e., the upstream value of the undisturbed flow. For a transcritical solution, with a transition at the top of the obstacle, there must be equality in Eq. (8), so that two roots of (7) coalesce at the summit. Hence symmetric solutions are possible only for obstacles of height $M \leqslant M_0$, where

$$M_0 = 1 + \frac{F^2}{2} - \frac{3}{2}F^{2/3}. \tag{9}$$

This equation defines the curve BAE in Fig. 2. The curve AG on the supercritical side arises because transcritical solutions can also exist within part of the supercritical region. Curve AG is the outer boundary of this hysteresis region (I/III), where the flow following a stationary jump exactly meets the transcritical solution over the obstacle. From (4) and (8), this occurs where

$$\frac{1}{2}(\sqrt{8F^2+1}-1) + \frac{2F^2}{(\sqrt{8F^2+1}-1)^2} = M_1 + \frac{3}{2}F^{2/3},$$

or where

$$M_1 = \frac{(8F^2+1)^{3/2}+1}{16F^2} - \frac{1}{4} - \frac{3}{2}F^{2/3}. \tag{10}$$

Finally the curve AD, which separates solutions with a jump on the downstream side of the obstacle (region IVb) from those without (region IVa), can be obtained from the following system of equations:

$$\begin{aligned}
&\mathcal{F} = \sigma_0 F - (\sigma_0 - 1)\sqrt{\frac{1}{2}\sigma_0(\sigma_0+1)},\\
&\sigma_i^3 - \left(M + \frac{3}{2}\mathcal{F}^{2/3}\right)\sigma_i^2 + \frac{1}{2}\mathcal{F}^2 = 0, \quad i=0,1, \quad \sigma_0 > 1,\\
&\qquad\qquad\qquad\qquad\qquad\qquad\qquad 0 < \sigma_1 < 1,\\
&\sigma_+ = \frac{1}{2}\sigma_1\left(\sqrt{\frac{8\mathcal{F}^2}{\sigma_1^3}+1}-1\right),\\
&\frac{\mathcal{F}}{\sigma_+} - 2\sigma_+ = F - 2.
\end{aligned} \tag{11}$$

System (11) can be solved numerically to obtain $F=F(M)$ (the dotted curve AD′ in Fig. 2), which defines the boundary between solutions with downstream recovery jumps on the obstacle from those without in the Baines scenario. Also obtained are σ_0 and σ_1, which are the layer thicknesses at the beginning and end of the obstacle, respectively, and σ_+, the layer thickness after the stationary hydraulic jump at the end of the obstacle. The curve AD, which is the relevant curve for the regime boundary of the rotating solutions in the limit $B \to 0$, is given by $F=\mathcal{F}(M)$ in the solution of (11). The differences between the Baines scenario and Fig. 2 arise because the steady-state equation (2) does not hold in the nonrotating transcritical regime. Hence, there is a blocking regime in the Baines picture to the right of curve AH′, defined by $\mathcal{F}=0$ in (11), which is entirely absent in the limit of weak rotation. In the derivation of (11) it is necessary to consider the properties of moving jumps and rarefaction waves, and the nondimensional mass flux over the obstacle $\mathcal{F}$ differs from the upstream and downstream mass flux F. In contrast, when even a small amount of rotation is present, steady solutions appear to be always attainable[7] and attention can be confined to the system (2) together with (3). As discussed by BL, the presence of rotation introduces a length scale into the system, the Rossby radius of deformation $L_R=c/f$, and the obstacle cannot influence the flow on scales greater than L_R. Instead, the flow undergoes geostrophic adjustment within this region to reach a state of geostrophic balance in which the pressure gradients associated with variations in the surface height are balanced by Coriolis forces on the jets in the along-ridge direction that have velocity v.

III. SEMIANALYTIC STEADY SOLUTIONS FOR ROTATING FLOWS OVER A PARABOLIC OBSTACLE

A. Method of construction of solutions

Much insight can be gained into flow over one-dimensional obstacles in the presence of rotation by restricting attention to parabolic obstacles. Considering an obstacle with

$$b = 4x(1-x), \quad 0 < x < 1,$$

Eq. (2) becomes

$$\left(\sigma + \frac{F^2}{2\sigma^2}\right)_{xx} + B(1-\sigma) = \begin{cases} 8M, & 0 < x < 1, \\ 0, & x < 0,\ x > 1, \end{cases} \qquad (12)$$

with the conditions at the edges of the obstacle being

$$\left(1 - \frac{F^2}{\sigma^3}\right)[\sigma_x]_-^+ = \begin{cases} -4M & \text{at } x=0, \\ +4M & \text{at } x=1. \end{cases} \qquad (13)$$

Equation (12) may be integrated once[20] to give

$$(\sigma_x)^2\left(1 - \frac{F^2}{\sigma^3}\right)^2 - B\left(\sigma^2 - 2\sigma + \frac{2F^2}{\sigma} - \frac{F^2}{\sigma^2}\right) = \begin{cases} K_0 & x < 0, \\ K_1 + 8M\left(2\sigma + \dfrac{F^2}{\sigma^2}\right) & 0 < x < 1, \\ K_2 & x > 1. \end{cases} \qquad (14)$$

From Eq. (14), solutions can be constructed in the phase plane (σ, σ_x). In the phase plane, solutions follow contours of constant K_i $(i=0,1,2)$ until they meet either the edge of the obstacle, as discussed below, or a stationary hydraulic jump where the solution leaps to a new position according to (5) and (6). As is clear from Eq. (14), the phase-plane contours have a different pattern above the obstacle $(0<x<1)$ compared to outside the obstacle. The solution therefore follows the "outside obstacle" set of contours until $x=0$, where $\sigma=\sigma_0$. Here the solution jumps to a new position in phase space according to (13), and then follows the "above obstacle" set of contours until $x=1$. At $x=1$, $\sigma=\sigma_1$ is determined by the condition

$$x(\sigma_1) - x(\sigma_0) = 1,$$

where

$$x(\sigma) = \int_{\sigma_0}^{\sigma} \frac{d\sigma}{\mathcal{G}(\sigma;K_1)}, \qquad (15)$$

and $\mathcal{G}(\sigma;K_1)$ is obtained by rearranging (14),

$$\sigma_x = \mathcal{G}(\sigma;K_1) = \pm \frac{\sigma^3}{\sigma^3 - F^2}\left[K_1 + B\left(\sigma^2 - 2\sigma + \frac{2F^2}{\sigma} - \frac{F^2}{\sigma^2}\right) + 8M\left(2\sigma + \frac{F^2}{\sigma^2}\right)\right]^{1/2}.$$

Note that σ need not necessarily be monotonic above the obstacle, in which case the integral expression (15) must be appropriately modified. Phase-plane contours may cross the $\sigma_x=0$ axis, and the opposite sign must then be taken for the function $\mathcal{G}(\sigma;K_1)$. Similarly, the shape of solutions before the obstacle may be determined from the equation

$$x(\sigma) = \int_{\sigma_0}^{\sigma} \frac{d\sigma}{\mathcal{F}(\sigma;K_0)}, \qquad (16)$$

with

$$\mathcal{F}(\sigma;K_0) = \pm \frac{\sigma^3}{\sigma^3 - F^2}\left[K_0 + B\left(\sigma^2 - 2\sigma + \frac{2F^2}{\sigma} - \frac{F^2}{\sigma^2}\right)\right]^{1/2}.$$

The shape of solutions after the obstacle may also be obtained using (16) with σ_1 and K_2 replacing σ_0 and K_0.

Figure 3 shows the regime diagrams for the solutions obtained at rotation rates corresponding to (a) $B=2$ and (b) $B=8$. These rotation rates are chosen in order to best illustrate the development of different regimes of solution from the nonrotating limit. The equations of the curves and the details of their derivation are given below. Figure 3 can be compared with BL's Fig. 6 where the numerically calculated regime diagram for a semi-infinite piecewise-linear ridge is presented at several different rotation rates. The regime diagram in Fig. 3 has, however, several different and important features that are not discussed in BL, aspects of which are not unique to the parabolic obstacle shape considered here, but are universal to all rotating flow over topography. In particular, the new issues addressed here are as follows:

(1) What controls the position and occurrence of a downstream hydraulic jump?
(2) What controls the amplitude of the wave train of nonlinear inertia-gravity waves downstream of the obstacle. Under what circumstances are waves of limiting amplitude generated?
(3) What happens to the region of hysteresis (AEG in Fig. 2) present in nonrotating flow. BL did not find such a region for the semi-infinite ridge considered in their study, even at very low rotation rates. Is this a special property of the piecewise linear function chosen for their obstacle?

Additionally, exact analytic expressions are given below for the supercritical and subcritical transition curves, and it is shown explicitly how these evolve as rotation is increased.

Examples of steady solutions constructed in the manner described above are given in Figs. 4–6, with the details of derivation described below. On the left-hand panels, contours of constant K_i are plotted, with the constant K_1 contours on the "above obstacle" solution shown as dotted curves, and the constant K_0 (or K_2) contours, corresponding to the solution away from the obstacle, as solid curves. The gray curves show the path of the solution in phase space, with important points such as the obstacle boundaries and jump positions being labeled. The right-hand panels illustrate the free surface heights $\sigma+Mb$ in the vicinity of the obstacle.

Transcritical flow occurs when the local Froude number passes through unity, or equivalently when $\sigma=F^{2/3}$ somewhere in the domain. Inspection of the phase-plane diagrams in Figs. 4–6 shows that the solution phase space is effectively divided into two by a vertical line at $\sigma=F^{2/3}$, with supercritical flow to the left and subcritical flow to the right. A single curve on both the "above obstacle" solution and another on the "away from obstacle" solutions passes through the $\sigma=F^{2/3}$ dividing line. These are the transcritical curves, and are plotted as the thick solid and thick dotted curves on each phase-space panel. The values of $K_1=K_{1c}$ and $K_0=K_{0c}$ (or $K_2=K_{2c}$) corresponding to the transcritical curves may be calculated by setting $\sigma_x=0$ in (14) and finding

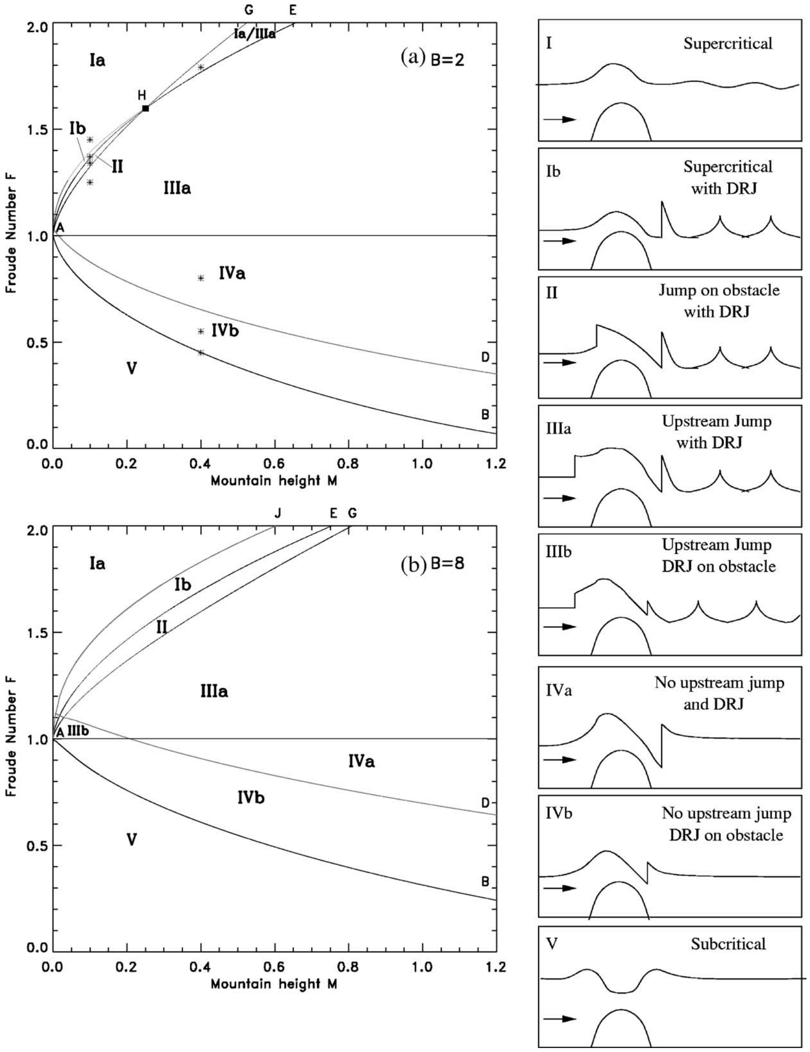

FIG. 3. Obstacle height/Froude number (M,F) regime diagrams for the steady solutions in the presence of rotation with (a) $B=2$ and (b) $B=8$. The regimes are as follows: (Ia) Supercritical flow everywhere. (Ib) Supercritical flow over obstacle with a stationary downstream recovery jump (DRJ). (II) Transcritical flow over obstacle with a jump on the obstacle and a DRJ. (IIIa) Transcritical flow over obstacle with an upstream jump and DRJ after the obstacle. (IIIb) Transcritical flow over obstacle with an upstream jump, and a DRJ on the obstacle. (IVa) Transcritical flow over obstacle with no upstream jump and a DRJ after the obstacle. (IVb) Transcritical flow over obstacle with no upstream jump and a DRJ on the obstacle. (V) Subcritical flow everywhere. The region labeled Ia/IIIa is a hysteresis region where more than one solution is possible. In the upper panel, stars mark the parameter settings of the solutions shown in Figs. 4–6.

the value of K_i for which the resulting quintic polynomial has a double root at $\sigma=F^{2/3}$. The following results are obtained:

$$K_{0c}=K_{2c}=3B(F^{2/3}-F^{4/3}),$$
$$K_{1c}=3B(F^{2/3}-F^{4/3})-24MF^{2/3}. \tag{17}$$

The equations of the transcritical curves are essential in the construction of the solutions as described below. The different qualitative solution regimes depend crucially on whether the flow is purely subcritical, purely supercritical, or, in the case where the flow is transcritical, where the flow switches between subcritical and supercritical relative to the obstacle. The nature of the transition between the different flow regimes is found to depend on the obstacle inverse Burger number $\mathcal{B}_m$, defined as

$$\mathcal{B}_m=\frac{B}{M}=\frac{f^2L^2}{gh}.$$

The different types of possible transitions are described in turn below.

B. Supercritical transition at rapid rotation rates $\mathcal{B}_m>8$

Here we consider the supercritical transition when rotation is sufficiently rapid so that the obstacle inverse Burger number $\mathcal{B}_m>8$. In parameter space, this corresponds to the region to the left side of point H $(M<0.25)$ in the regime diagram Fig. 3(a), and everywhere illustrated in Fig. 3(b) $(M<1)$. The derivation of the location of point H and the $\mathcal{B}_m>8$ criterion is discussed below.

Steady solutions illustrating the supercritical transition for $M=0.1$, $B=2$ are shown in Fig. 4. The four cases $F=1.45$, $F=1.37$, $F=1.35$, and $F=1.25$ show the progression between solution regimes Ia, Ib, II, and IIIa in Fig. 3(a), as labeled there by stars. On the left panels, the solution is illustrated in phase space (σ,σ_x), while the right panels show the free surface height $\sigma+Mb$ of the flow over the obstacle. For those branches of the solution where exact closed-form analytic expressions are not available, the shape of the solution is obtained by evaluating the integrals (15) and (16)

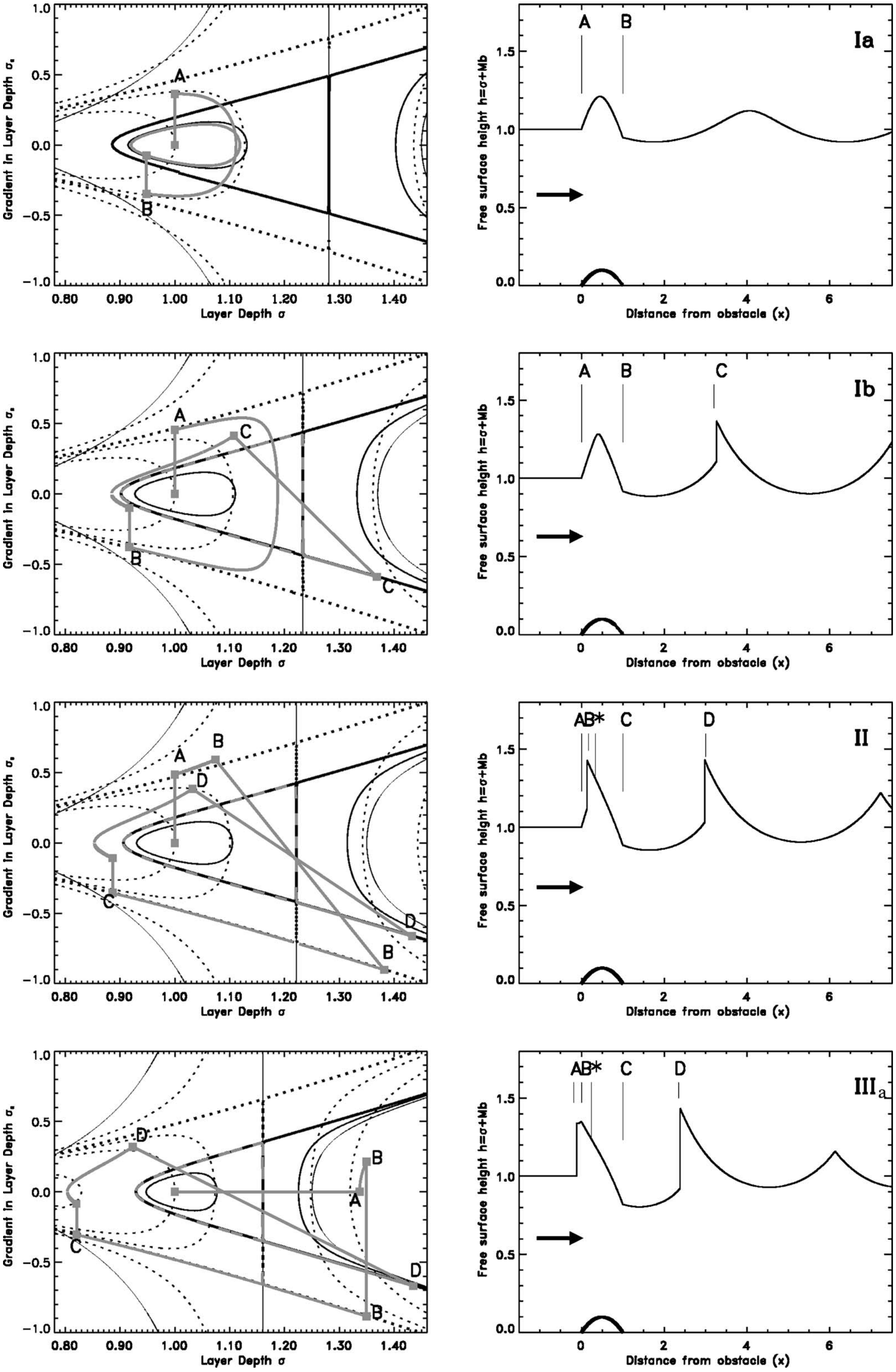

FIG. 4. Illustrating the steady solutions as they appear in (σ,σ_x) phase space (left panels) and free-surface height near the obstacle (right panels). The parameter settings are $B=2$, $M=0.1$, and (Ia) $F=1.45$, (Ib) $F=1.37$, (II) $F=1.35$, and (IIIa) $F=1.25$. In the phase-space panels, the dotted curves are contours of constant K_1, and the solid curves of constant K_0 (K_2) with transcritical curves emphasized in bold. The gray curves show the solution itself. For transcritical flows, the location of the critical point on the obstacle controlling the flow (where $\sigma=F^{2/3}$) is labeled by a star.

using a fourth-order Runge-Kutta algorithm. Below, to illustrate in detail the application of methodology introduced above, the derivation of the solutions for the Ia, Ib, II, and IIIa solutions are described. In each case, when $F>1$ ahead of the obstacle or initial jump, the flow is supercritical everywhere and inertia-gravity waves cannot propagate upstream. Hence $\sigma=1$, $\sigma_x=0$ up to the edge of the obstacle at $x=0$ or an initial hydraulic jump.

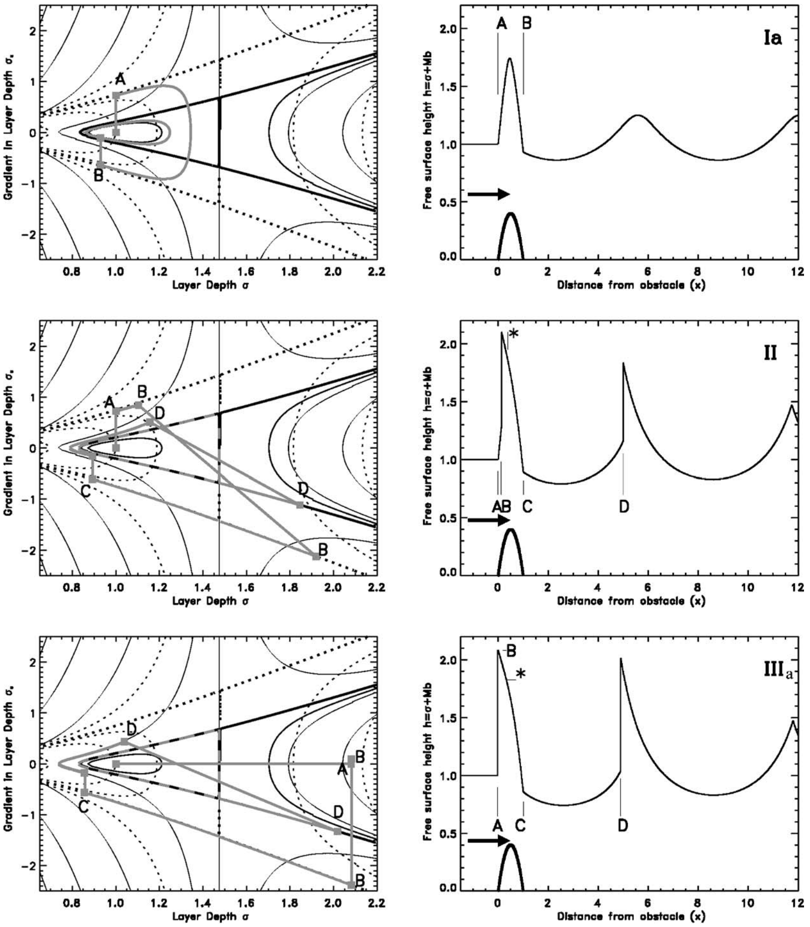

FIG. 5. As Fig. 4 but illustrating the three possible steady solutions (Ia, II, IIIa) in the hysteresis region (labeled Ia/IIIa) when $B=2$, $M=0.4$, and $F=1.79$. The purely supercritical solution (Ia) and the transcritical solution with upstream jump (IIIa) are stable, but the transcritical solution with a jump on the obstacle (II) is unstable.

Solutions with entirely supercritical flow over the obstacle, i.e., in parameter regimes Ia and Ib, are constructed as follows. At the obstacle edge ($x=0$, $\sigma_0=1$), the solution jumps in phase space according to (13) to the point A, which lies on the "above obstacle" solution curve with $K_1=K_{1o}$, where

$$K_{1o} = 16M^2 + B(1-F^2) - 16M - 8MF^2.$$

The solution follows this curve in phase space, crossing the $\sigma_x=0$ axis until it reaches point B where $x=1$, $\sigma=\sigma_1$, with σ_1 given by the root of

$$x(\sigma_1) + x(1) - 2x(\sigma_m) = 1. \tag{18}$$

Here $x(\sigma)$ is determined from the integral (15), with the positive sign taken for $\mathcal{G}$, and σ_m is the maximum thickness on this branch of the solution, given by the largest real root of

$$B(\sigma^4 - 2\sigma^3 + 2F^2\sigma - F^2) + 8M(2\sigma^3 + F^2) + K_{1o}\sigma^2 = 0.$$

At point B, the spatial gradient σ_x changes according to (13) as the solution has reached the rear edge of the obstacle. Subsequently, the solution follows a contour of constant K_2 on the "away from obstacle" solution (solid black contours), with the value of K_2 calculable from (14). Two possibilities exist. If the flow is to remain entirely supercritical, as it does throughout region Ia in Fig. 3, we must have $K_2 \leq K_{2c}$, in which case a contour of constant K_2 forms a closed orbit as illustrated in Fig. 4 (Ia). This closed orbit corresponds to a wave train of finite-amplitude inertia-gravity waves downstream of the obstacle.

An alternative possibility is that $K_2 > K_{2c}$ (this possibility corresponds to region Ib in Fig. 3, and an example of the resulting solution is shown in Fig. 4, on the Ib panel). In this case, the solution can no longer follow a closed orbit after the obstacle, and must undergo a hydraulic jump to subcritical flow at some point after the obstacle. The point C at which this takes place is uniquely determined by the condition that the solution after the jump must lie on the transcritical curve with $K_2=K_{2c}$. The transcritical curve is the only curve that allows the solution to return to supercritical, after which the solution describes inertia-gravity waves with limiting amplitude. On this transcritical curve, a closed-form expression for the solution shape has been obtained by integrating Eq. (16),[17] the derivation of which is discussed in the Appendix. The exact form of the wave shape is given by Eq. (A1). In physical terms, the region Ib solution therefore involves a downstream jump followed by an infinite wave train of limiting amplitude inertia-gravity waves. The transition between regimes Ia and Ib, corresponding to the appearance of the downstream jump, and given by the gray curve AH on Fig. 3(a) and AJ on Fig. 3(b), is derived by solving iteratively to obtain the value of M for which $K_2=K_{2c}$ at fixed values of F.

Consideration of the above methodology allows the derivation of the equation of the supercritical transition curve AE

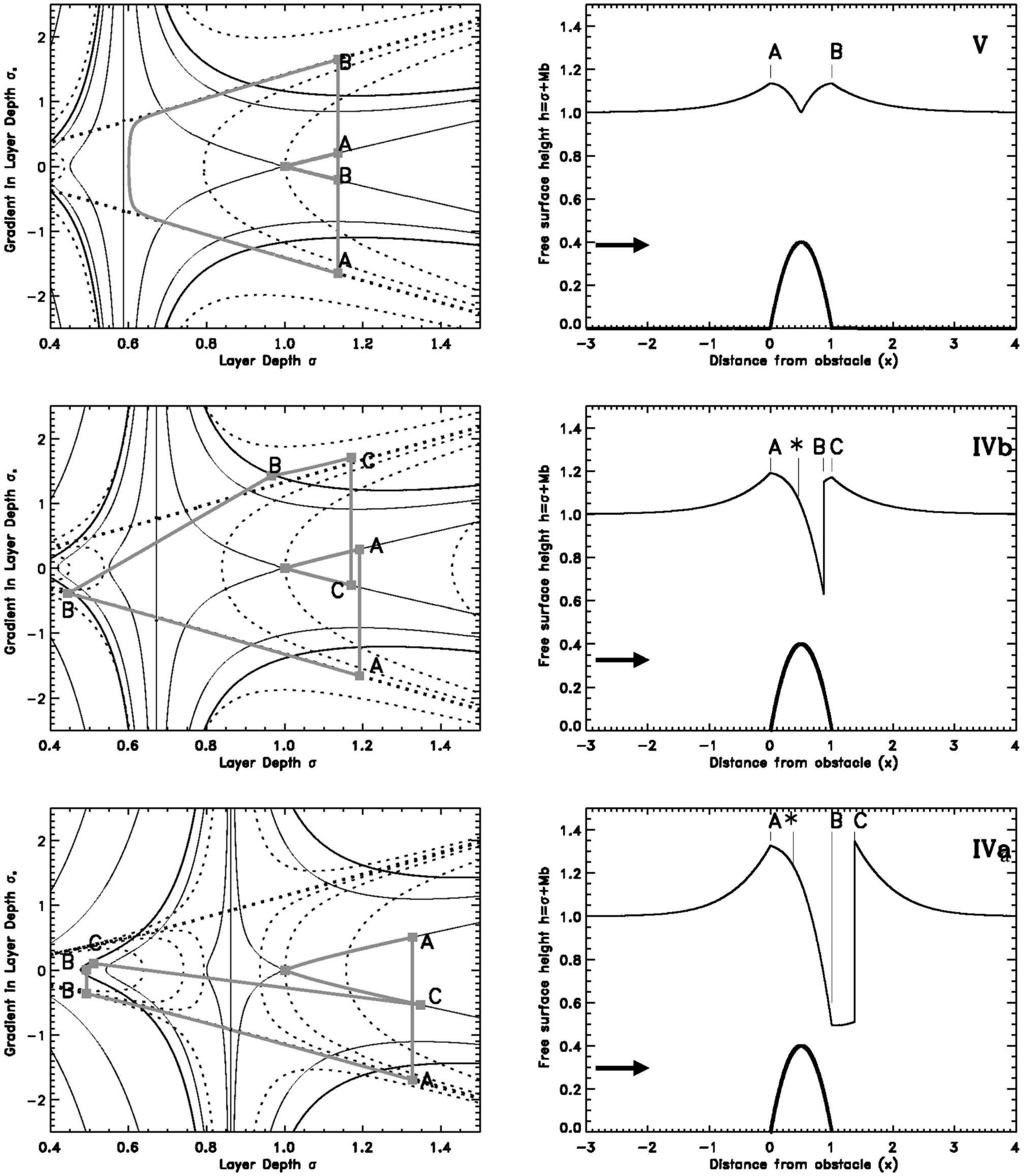

FIG. 6. As Fig. 4 but for the initially subcritical flows with $B=2$, $M=0.4$, and with (V) $F=0.45$, (IVb) $F=0.55$, and (IVa) $F=0.8$.

illustrated in the regime diagrams of Fig. 3. Supercritical flow as in regimes Ia/b is possible if and only if $K_{1o} \leqslant K_{1c}$, or

$$16M^2 + B(1-F^2) - 16M - 8MF^2 \leqslant 3B(F^{2/3} - F^{4/3}) - 24MF^{2/3}.$$

Curve AE is defined by equality in the above equation, which may be rearranged to yield

$$M = \hat{M}_0 = \frac{M_0}{2} + \frac{1}{2}\left[M_0^2 + \frac{B}{4}(F^{2/3} - 1)^3\right]^{1/2}, \qquad (19)$$

where $M_0 = M_0(F)$ is the nonrotating expression (9) for the curve AE. Clearly, $\hat{M}_0 \rightarrow M_0$ as $B \rightarrow 0$.

In regime II of Fig. 3, located between curves AE and AJ and to the left of point H, the only possible solution includes a jump on the obstacle. At the leading edge of the obstacle, the solution jumps in phase space to follow $K_1=K_{1o}>K_{1c}$. It is clear from the phase-plane diagram that the solution cannot continue indefinitely on this curve and must jump to subcritical flow. The position at which this occurs, labeled point B in phase space and with thickness σ_-, is defined by

$$2(B-8M)\left(\sigma_+ + \frac{F^2}{2\sigma_+^2} - \sigma_- - \frac{F^2}{2\sigma_-^2}\right) = K_{1c} - K_{1o}, \tag{20}$$

together with (5), since the solution must join the transcritical curve ($K_1=K_{1c}$). Along this curve, the solution returns to supercritical flow, and thereafter behaves as a regime Ib flow with a further jump after the obstacle.

The solution in regime IIIa, corresponding to transcritical flow with an upstream jump, is constructed as follows. The initial jump must satisfy (5), which determines the thickness after the jump $\sigma_+=(\sqrt{1+8F^2}-1)/2$ (point A in phase space). The solution then follows a path of constant K_0, where

$$K_0 = -B\left(\sigma_+^2 - 2\sigma_+ + \frac{2F^2}{\sigma_+} - \frac{F^2}{\sigma_+^2}\right),$$

on the "away from obstacle" solution (solid black contours) until it reaches point B at the edge of the obstacle ($x=0$, $\sigma=\sigma_0$). Point B is uniquely defined as it is the only possible point where the solution may join the transcritical solution over the obstacle (i.e., the thick dotted curve, with $K_1=K_{1c}$). Therefore, σ_0 must satisfy

$$\sqrt{\left[K_{1c} + B\left(\sigma_0^2 - 2\sigma_0 - \frac{2F^2}{\sigma_0} + \frac{F^2}{\sigma_0^2}\right) + 8M\left(2\sigma_0 + \frac{F^2}{\sigma_0^2}\right)\right]} + \sqrt{\left[K_0 + B\left(\sigma_0^2 - 2\sigma_0 - \frac{2F^2}{\sigma_0} + \frac{F^2}{\sigma_0^2}\right)\right]} - 4M = 0.$$

After reaching the obstacle edge, the solution follows the contour of constant $K_1=K_{1c}$. As shown in the Appendix, Eq. (15) can be integrated for $K_1=K_{1c}$ to give a closed analytic expression (A2) for the shape of the free surface over the obstacle in the case of the transcritical branch of the flow. Point C ($x=1$, $\sigma=\sigma_1$) is therefore given by the root of $x(\sigma_1)-x(\sigma_0)=1$, with $x(\sigma)$ given by (A2). As with supercritical flow, Eq. (13) may then be used to find the initial value of K_2 for the "after the obstacle" solution. For the cases examined ($B=2$ and $B=8$), it was invariably found that $K_2>K_{2c}$, so that a downstream jump is present after the obstacle throughout region IIIa. However, the possibility that transcritical solutions exist for other values of B in which no downstream jump is necessary has not been ruled out.

The equation of the regime diagram curve AG, separating regimes II and IIIa in parameter space, as well as the location [point H in Fig. 3(a)] of its intersection with AE, can be derived as follows. Transcritical flow with an upstream jump is possible only if the value of K_1 from a stationary jump located exactly at the obstacle boundary $x=0$ satisfies $K_1 \leqslant K_{1c}$, or

$$K_1 = 16M^2 - B\left(\sigma_+^2 - 2\sigma_+ + \frac{2F^2}{\sigma_+} - \frac{F^2}{\sigma_+^2}\right) - 8M\left(2\sigma_+ + \frac{F^2}{\sigma_+^2}\right) \leqslant 3B(F^{2/3} - F^{4/3}) - 24MF^{2/3},$$

where $\sigma_+=(\sqrt{8F^2+1}-1)/2$, as above. The curve AG is determined by equality in this equation (i.e., $K_1=K_{1c}$), which may be rearranged to give

$$M = \hat{M}_1 = \frac{M_1}{2} + \frac{1}{2}\left[M_1^2 + \frac{B}{4}(1 + 2F^2 - 3F^{4/3} - 2M_1)\right]^{1/2}, \tag{21}$$

where $M_1=M_1(F)$ is the nonrotating result (10) for the curve AG. Again, $\hat{M}_1 \to M_1$ as $B\to 0$. Note that corrections due to rotation differ significantly in magnitude for curves AE and AG, for example in Fig. 3(b) AG and AE have flipped positions compared with their positions in the nonrotating regime diagram (Fig. 2).

Next, consider the location of point H in Fig. 3(a). It is straightforward to demonstrate that if $B=8M$, then $\hat{M}_0=\hat{M}_1=(1+2F^2-3F^{4/3})/2$, that is, curves AE and AG meet at point H, where $M=B/8$. To the left of point H in Fig. 3(a), where $\mathcal{B}_m=B/M>8$, the supercritical transition is clearly different in nature from that to the right (where $\mathcal{B}_m<8$, and discussed below), as curves AE and AG are encountered in the opposite order. Interestingly $\mathcal{B}_m$, and hence the type of supercritical transition which occurs, is entirely independent of the depth H of the layer of the oncoming flow.

The $\mathcal{B}_m>8$ transition described above can be summarized as follows: As the Froude number is decreased, the amplitude of inertia-gravity waves generated downstream increases until the limiting amplitude is reached, and a hydraulic jump of initially infinitesimal size appears downstream of the obstacle. This downstream jump grows in amplitude as F is decreased further. Next, an upstream jump appears on the obstacle, just ahead of the critical point where $\sigma=F^{2/3}$, and moves upstream until it reaches the edge of the obstacle. At this point, the upstream jump has maximum amplitude. As F is further decreased, the upstream jump decreases in amplitude as it moves ahead of the obstacle, finally reaching zero amplitude at $F=1$ where the flow evolves smoothly into a regime IV solution as described in the subcritical discussion below.

C. Supercritical transition and hysteresis at weaker rotation rates $\mathcal{B}_m<8$

If the obstacle inverse Burger number $\mathcal{B}_m<8$, the supercritical transition has a different character from that described above, and in fact resembles the supercritical transition in the nonrotating case. In the nonrotating case (Fig. 2), there is a region of hysteresis AEG where there are two possible stable solutions, corresponding to regimes I and IIIa, respectively. There is also known to be a third unstable solution, as recently shown by Baines and Whitehead,[28] with an upstream jump on the obstacle. This belongs to the regime II (upstream jump on the obstacle) class of solutions described above. Pratt[29] has shown that the type of steady solution that emerges in region I/IIIa depends on how the flow is initialized. If the upstream Froude number F is subsequently changed to leave the hysteresis region I/IIIa, causing the preexisting flow solution to be no longer permissible, the flow can undergo an abrupt, finite-amplitude transition to the opposite solution. It is the suppression by rotation of these abrupt changes that is the remarkable feature of the $\mathcal{B}_m > 8$ supercritical transition described above.

In the case of rotating flow, the hysteresis region is reduced in size to HEG in Fig. 3(a), and exists only for $M \geqslant 1$ when $B \geqslant 8$ [e.g., Fig. 3(b)]. Figure 5 shows the three solutions that may be constructed for parameters $B=2$, $F=1.79$, and $M=0.4$ in the hysteresis region. The method of construction is essentially identical to the regime Ia, II, and IIIa solutions described above, with the distinction that the analytic expression for transcritical flow over the obstacle is given by (A4) rather than (A2). As in the nonrotating case, the "jump on the obstacle" solution (middle panel) may be shown to be unstable.

The stability of the "upstream jump on the obstacle" solutions in regions II and I/IIIa of the regime diagram can be investigated explicitly as follows. Suppose for a given stationary solution the jump is at position $x=x_J \in [0,1]$ (i.e., on the obstacle). A "nearby" stationary solution with a jump at $x=x_J+\delta x$ may be constructed by introducing a (small) impulsive force (per unit depth) $I\delta(x-x_J-\delta x)/\sigma$ on the right-hand side of the x-momentum equation (1), applied at the jump location. The jump condition (4) is modified to

$$\left[\frac{\sigma^2}{2}+\frac{F^2}{\sigma}\right]_-^+ = I,$$

and this can be used together with the fact that any steady solution with a jump on the obstacle must jump in the phase plane from $K_1=K_{1o}$ to $K_1=K_{1c}$ [as in Eq. (20)], to determine a relationship between I and the displacement of the jump δx,

$$I = \delta x \frac{B-8M}{(\sigma_+-1)B+8M}(\sigma_+-\sigma_-)\sigma_-\sigma_{x-}\left(\frac{F^2}{\sigma_-^3}-1\right). \qquad (22)$$

It is clear from (22), since $\sigma_{x-}(F^2/\sigma_-^3-1)>0$ and $\sigma_+>1$, that a restoring impulsive force is necessary to maintain the "nearby" steady solution if $B<8M$ ($\mathcal{B}_m<8$), indicating that in its absence the jump would propagate away from x_J, and therefore that the initial stationary solution is unstable. By contrast, if $B>8M$ ($\mathcal{B}_m>8$), the impulsive force necessary to maintain the nearby solution is directed away from the initial jump location, indicating that in its absence the jump would return to its original position, and therefore that the initial steady solution is stable. The stability of nonrotating jumps over the obstacle ($\mathcal{B}_m=0$) has been investigated by Baines and Whitehead,[28] who employed different arguments to show that, as found here, the upstream jump on the obstacle solution is unstable.

D. Subcritical transition and downstream recovery jump location

Figure 6 shows steady solutions constructed for subcritical oncoming flow, $F<1$. The nondimensional mountain height $M=0.4$, the flow inverse Burger number $B=2$, and $F=0.45$, 0.55, and 0.8 in the three panels, respectively. The three solutions illustrate the three different possible regimes: entirely subcritical flow (V), transcritical flow with no upstream jump and a recovery jump on the obstacle (IVb), and transcritical flow with no upstream jump and a recovery jump after the obstacle (IVa).

It is possible to deduce from the phase-space diagram in Fig. 6 that if the flow is to remain entirely subcritical over the obstacle, then it must also be symmetric over the obstacle. In subcritical flow, as $x \to \pm\infty$ the flow must return to its undisturbed state with $\sigma=1$, $\sigma_x=0$, since there are no closed curves on the subcritical side of the phase plane. The "away from obstacle" solutions therefore have $K_0=K_2=B(1-F^2)$. At the edge of the obstacle $x=0$ the solution must "jump" in phase space according to (13) onto an over the obstacle curve with constant $K_1<K_{1c}$, and follow this curve until it jumps back at $x=1$ according to the same condition onto a curve with constant $K_2=K_0$. As the change $K_1-K_0=K_1-K_2$ may be shown to be a monotonic function of σ in the relevant region, the $x=0$ and $x=1$ transitions must occur at the same value of σ (i.e., $\sigma_0=\sigma_1$), rendering the whole solution symmetric. The solution is entirely determined by the further condition that

$$x(\sigma_0)-x(\sigma_m)=\tfrac{1}{2},$$

where $x(\sigma)$ is given by (15), and σ_m is the minimum value of σ along the curve with K_1 determined from (3).

The curve describing the transition between subcritical and transcritical flow on the (M,F) diagram corresponds to the situation where $K_1=K_{1c}$. In this case,

$$\begin{aligned}&\sqrt{\{B[\sigma_0^4-2\sigma_0^3+3(F^{2/3}-F^{4/3})\sigma_0^2+2F^2\sigma_0-F^2]+8M(2\sigma_0^3-3F^{2/3}\sigma_0^2+F^2)\}}\\&\qquad+\sqrt{\{B[\sigma_0^4-2\sigma_0^3+(1-F^2)\sigma_0^2+2F^2\sigma_0-F^2]\}}-4M\sigma_0=0,\\&x(\sigma_0)-x(F^{2/3})=\tfrac{1}{2},\end{aligned} \qquad (23)$$

where Eq. (A2) or (A4) is used to evaluate $x(\sigma)$, depending on whether the obstacle Burger number $\mathcal{B}_m$ is less than or greater than 8. This system can be readily solved numerically using the secant method to find M and σ_0 given (F,B), and hence obtain the curve. In the nonrotating case $(B=0)$, it is straightforward to evaluate (15) directly and show that $\sigma_0=1$, and thus that $M=M_0(F)$ with M_0 given by (9).

The other main feature on the subcritical side of the regime diagram is the curve separating solution regime IVa (recovery jump after obstacle) and IVb (recovery jump on obstacle). The location of this curve is determined by assuming a stationary jump at the downstream edge of the obstacle, resulting in the following system of equations, where σ_0 also satisfies the first equation in set (23):

$$x(\sigma_1) - x(\sigma_0) = 1,$$

$$\sigma_+ = \sigma_+ = \frac{\sigma_1}{2}\left(\left[\frac{8F^2}{\sigma_1^3} + 1\right]^{1/2} - 1\right), \tag{24}$$

$$\begin{aligned}&\sqrt{[K_+\sigma_+^2 + B(\sigma_+^4 - 2\sigma_+^3 + 2F^2\sigma_+ - F^2) + 8M(2\sigma_+^3 + F^2)]}\\&\quad + \sqrt{\{B[\sigma_+^4 - 2\sigma_+^3 + (1-F^2)\sigma_+^2 + 2F^2\sigma_+ - F^2]\}}\\&\quad - 4M\sigma_+ = 0,\end{aligned}$$

where $K_+=K_{1c}+(B-8M)(2\sigma_+ + F^2/\sigma_+^2)$, and $x(\sigma)$ is evaluated from (A2) or (A4) as appropriate. Note that the curve defined by the set (24) converges to the curve AD in Fig. 2 when $B\to 0$, and not to AD′, which is the relevant curve in Baines's nonrotating regime diagram. This is because no matter how low the rotation rate, the mass flux over the obstacle in a rotating steady solution is always equal to the upstream mass flux. This is not true for the nonrotating quasisteady solutions in Baines's problem.

Increasing the rotation rate, i.e., increasing B while maintaining F and M, has an effect on the solutions as follows. The most obvious effect is to reduce the horizontal scale of the response relative to the obstacle length L, which as discussed above scales according to the Rossby radius $(B^{-1/2}L)$. Upstream and downstream stationary jumps, if present, move closer to the obstacle until, as B is increased further, they move on to the obstacle itself and decay in amplitude until they vanish entirely. For $F>1$ the wavelength of limiting amplitude inertia-gravity waves generated downstream of the obstacle is reduced with increasing rotation, although their amplitude is unchanged.

IV. NUMERICAL VALIDATION AND INVESTIGATION OF THE REGION OF HYSTERESIS

In order to validate the steady solutions derived above, including their stability properties, a shock-capturing, finite-volume numerical code was employed to solve the time-dependent, rotating shallow water equations (1), following LeVeque.[30] A grid of 10000 points was employed to discretize the domain from $x=-5$ to $x=10$, with the incoming mass flux specified at $x=-5$ and an outflow condition at $x=10$. The model was integrated forward in time with initial conditions of a flat interface $\sigma+Mb=1$ and constant relative velocity $(u,v)=(F,0)$ (except where otherwise stated below), until a rigorous steady-state numerical criterion was satisfied. The steady solutions shown in Figs. 4 and 6 were reproduced with errors in jump position on the order of 10^{-2} and errors in surface height typically of the order of 10^{-4}.

The time-dependent numerical model is of further use in investigating convergence to the steady solutions, corresponding to the hysteresis region (Ia/IIIa), shown in Fig. 5. Figure 7 shows the time evolution of the flow with $B=2$, $F=1.79$, and $M=0.4$ with two different initial conditions. Both the free surface height $h=\sigma+Mb$ and the along-obstacle velocity v are shown. As shown by Pratt,[29] in the nonrotating hysteresis region I/IIIa shown in Fig. 2, the solution converges to one or another of the two stable solutions depending on the initial conditions. This sensitivity to the initial conditions is explicitly demonstrated for the rotating case in Fig. 7, where the gray curves show the evolution of the numerical solution from the initial conditions at $t=0$ (dotted curves) to the steady solutions constructed as in Fig. 5 (black curves). In the top panel, the initial conditions correspond to a flat interface and uniform flow, as described above, and the solution converges to the supercritical solution (Ia). In the lower panel, the initial conditions consist of the steady state obtained from the model for a larger mountain $(M=0.6)$. In this latter case, the solution converges to the transcritical solution (IIIa).

Several promising new numerical algorithms have been recently developed to include efficiently the nonconservative topographic and rotation terms using Gudonov-type methods.[31,32] The exact analytical transcritical solutions (A2) and (A4) should prove to be useful in developing computational tests for these algorithms.

V. CONCLUSIONS

Solutions for flow over a one-dimensional parabolic obstacle in rotating single-layer and one-and-a-half layer fluids have been presented. Analytical expressions for the regime boundaries defining the various qualitative solutions have been determined, for both supercritical and subcritical flow. As pointed out by Baines and Leonard[7] (BL herein), rotation has the effect of increasing the range of flow speeds for which purely supercritical or subcritical solutions are possible. Perhaps the most striking new feature discovered here is the change in the nature of the supercritical transition depending on whether the nondimensional obstacle inverse Burger number $\mathcal{B}_m=f^2L^2/gh$ is greater than or less than 8. For $\mathcal{B}_m>8$, rotation is found to suppress hysteresis, and the transition from supercritical to transcritical flow is characterized by the gradual emergence of hydraulic jumps ahead of and behind the obstacle, rather than an abrupt transition from a jump-free solution to a solution with a finite-amplitude jump. Interestingly, $\mathcal{B}_m$, and hence the type of supercritical

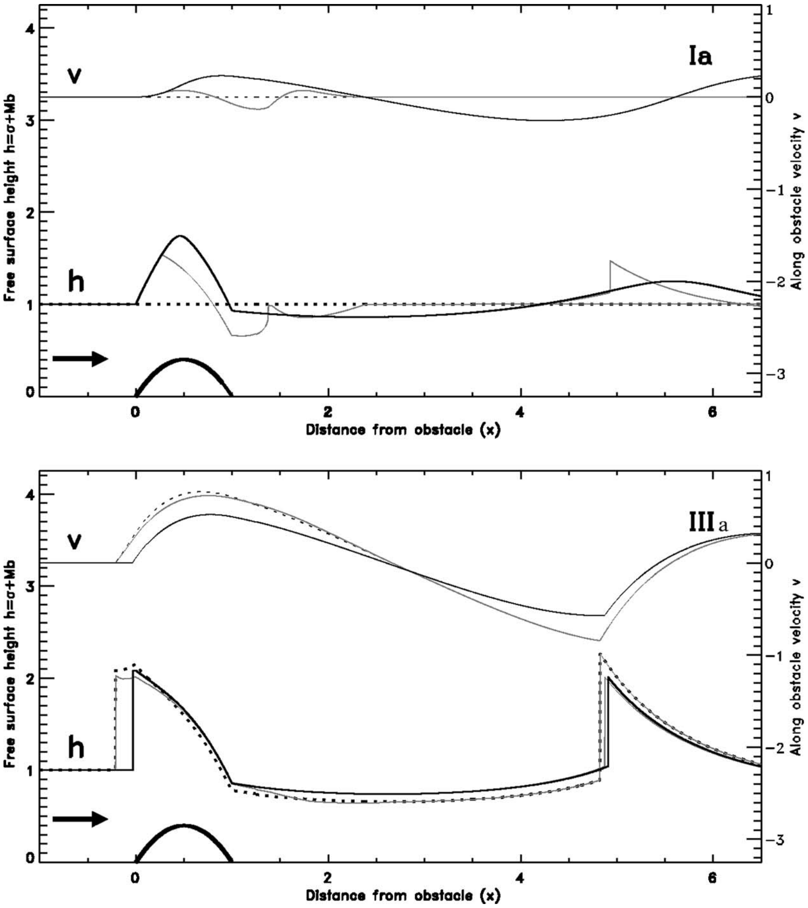

FIG. 7. Illustrating convergence to different stable steady solutions within the hysteresis region ($B=2$, $M=0.4$, $F=1.79$). The top panel shows the flow evolving toward the supercritical steady solution (Ia, solid black curve) from an initial condition of a flat surface (dotted line). The evolution of both the free-surface height $h=\sigma+Mb$ (lower curves) and the along-obstacle velocity v (upper curves) is shown in each case. The gray curves in both panels show the time-dependent numerical solution at nondimensional times $t=0.25, 4$. The bottom panel shows the solution evolving toward the transcritical solution (IIIa), from an initial condition as described in the text (dotted curve).

transition, is independent of the layer depth H of the oncoming flow. It seems likely, and initial numerical simulations with different ridge-like obstacles seem to confirm this, that a similar condition on $\mathcal{B}_m$ holds for other obstacle shapes. An exception may be the semi-infinite, piecewise-linear ridge investigated numerically by BL, as they did not discover a region of hysteresis at low rotation rates.

It is hoped that these solutions will be instructive to researchers investigating atmospheric and oceanic flows over topography in both two and three dimensions, and also in the study of the boundary layer flows in the vicinity of oncoming cold fronts.[15] A further application concerns the interpretation of rotating tank towing experiments.[9,10] One of the main results of the latter study was the identification of a large-amplitude wave on the downstream side of the obstacle, followed by a wave train of inertia-gravity waves. Another interesting question concerns the location and amplitude of solitary waves, relative to the location of the hydraulic jumps discussed herein, when near-critical shallow water flow is regularized by dispersion, as in the Ostrovsky equation[11–13] in both one- and two-dimensional flows. Finally, the closed-form analytic solutions for transcritical flow over the parabolic obstacle discovered may prove useful as a test case for shock-permitting numerical schemes that seek to solve systems of partial differential equations, such as (2), which cannot easily be written in conservative form.[31,32]

ACKNOWLEDGMENTS

The authors would like to thank Peter Baines for a helpful discussion, as well as the two anonymous reviewers for their insightful comments.

APPENDIX: CLOSED-FORM SOLUTIONS FOR TRANSCRITICAL FLOWS AND INERTIA-GRAVITY WAVES OF LIMITING AMPLITUDE

Closed-form solutions for nonlinear inertia-gravity waves of limiting amplitude, corresponding to exact solutions of (16) with $K_2=K_{2c}$, have been given by Grimshaw *et al.*.[17] The solutions can be obtained because when $K_2=K_{2c}$, i.e., on the transcritical curve, each term in Eq. (14) is divisible by $(\sigma-F^{2/3})^2$. It is straightforward to integrate the resulting equation to obtain closed-form solutions for the shape of the free surface in the form $x=x(\sigma;B,F)$. The same technique may also be applied to Eq. (15) when $M\neq 0$ to obtain solutions for transcritical flow over the obstacle.

Grimshaw *et al.*'s solution for the limiting wave shape is, for $\mu=F^{2/3}$, given by

$$x - x_0 = \pm \frac{1}{\sqrt{B}}\left[\log 2\{\sqrt{\sigma^2 + 2(\mu-1)\sigma - \mu} + \sigma + \mu - 1\} + \frac{\mu}{\sigma}\sqrt{\sigma^2 + 2(\mu-1)\sigma - \mu} + \mu^{3/2}\sin^{-1}\left\{ \frac{(\mu-1)\sigma - \mu}{\sigma\sqrt{\mu^2 - \mu + 1}} \right\} \right], \tag{A1}$$

meaning that the waves have a nondimensional amplitude

$$a = 2\mu - 1 - \sqrt{\mu^2 - \mu + 1}.$$

In terms of a nondimensional wavelength Λ this leads to a dispersion relation for the nonlinear waves of the form $\Lambda = \Lambda(\mu)$,

$$\frac{\Lambda\sqrt{B}}{2} = \log \frac{\sqrt{3\mu(\mu-1)} + 2\mu - 1}{\sqrt{\mu^2 - \mu + 1}} + \sqrt{3\mu(\mu-1)} + \mu^{3/2}\sin^{-1}\left\{ \frac{(\mu-2)}{\sqrt{\mu^2 - \mu + 1}} + \frac{\pi}{2} \right\}.$$

When $M \neq 0$, Eq. (15) may be integrated to find analytic expressions for the transcritical flow over a parabolic ridge. Different solutions exist depending on the value of the obstacle inverse Burger number $\mathcal{B}_m$ defined above. Define $\kappa = 8/\mathcal{B}_m = 8M/B$. Then for $0 \leqslant \kappa < 1$,

$$x - x_0 = \pm \frac{1}{\sqrt{B}}\left[\log 2\{\sqrt{C(\sigma)} + \sigma + \mu + \kappa - 1\} + \frac{\mu\sqrt{C(\sigma)}}{\sigma(1-\kappa)} + \left(\frac{\mu}{1-\kappa}\right)^{3/2}\sin^{-1}\left\{ \frac{(\mu+\kappa-1)\sigma - \mu(1-\kappa)}{\sigma\sqrt{\mu^2 - \mu(1-\kappa) + (1-\kappa)^2}} \right\} \right], \tag{A2}$$

whereas for $\kappa = 1$,

$$x - x_0 = \pm \frac{1}{\sqrt{B}}\left(\log 2\{\sqrt{\sigma^2 + 2\mu\sigma} + \sigma + \mu\} - \frac{(2\sigma + \mu)\sqrt{\sigma + 2\mu}}{3\sigma^{3/2}} \right), \tag{A3}$$

and for $\kappa > 1$,

$$x - x_0 = \pm \frac{1}{\sqrt{B}}\left[\log 2\{\sqrt{C(\sigma)} + \sigma + \mu + \kappa - 1\} - \frac{\mu\sqrt{C(\sigma)}}{\sigma(\kappa-1)} + \left(\frac{\mu}{\kappa-1}\right)^{3/2} \times \log\left\{ \frac{2\sqrt{\mu(\kappa-1)}[(\mu+\kappa-1)\sigma + \mu(\kappa-1) + \sqrt{\mu(\kappa-1)C(\sigma)}]}{\sigma\mu^3} \right\} \right], \tag{A4}$$

with $C(\sigma) = \sigma^2 + 2(\mu+\kappa-1)\sigma - \mu(1-\kappa)$ in each case. Inserting $\kappa = 0$ into (A2) recovers the limiting amplitude nonlinear waveform of Grimshaw *et al.*[17]

[1] P. G. Baines, *Topographic Effects in Stratified Flows* (Cambridge University Press, Cambridge, 1995).

[2] Q. Jiang and R. B. Smith, "V-waves, bow shocks, and wakes in supercritical hydrostatic flow," J. Fluid Mech. **406**, 27 (2000).

[3] C. C. Mei, *The Applied Dynamics of Ocean Surface Waves* (World Scientific, Singapore, 1989).

[4] P. Queney, "The problem of airflow over mountains. A summary of theoretical studies," Bull. Am. Meteorol. Soc. **29**, 16 (1948).

[5] R. T. Pierrehumbert, "Linear results on the barrier effects of mesoscale mountains," J. Atmos. Sci. **41**, 1356 (1984).

[6] E. Sambuco and J. A. Whitehead, "Hydraulic control by a wide weir in a rotating fluid," J. Fluid Mech. **73**, 521 (1976).

[7] P. G. Baines and B. P. Leonard, "The effects of rotation on flow of a single layer over a ridge," Q. J. R. Meteorol. Soc. **115**, 293 (1989).

[8] L. J. Pratt, K. R. Helfrich, and E. P. Chassignet, "Hydraulic adjustment to an obstacle in a rotating channel," J. Fluid Mech. **404**, 117 (2000).

[9] T. Maxworthy, G. C. Dhieres, and H. Didelle, "The generation and propagation of internal gravity waves in a rotating fluid," J. Geophys. Res. **89**, 6383 (1984).

[10] E. R. Johnson, J. G. Esler, O. J. Rump, J. Sommeria, and G. G. Vilenski, "Orographically generated nonlinear waves in rotating and nonrotating two-layer flow," Proc. R. Soc. London, Ser. A (in press).

[11] G. G. Vilenski and E. R. Johnson, "Near critical free-surface rotating flow over topography," Proc. R. Soc. London, Ser. A **460**, 2865 (2004).

[12] L. A. Ostrovsky, "Approximate methods in the theory of nonlinear waves," Radiophys. Quantum Electron. **17**, 344 (1974).

[13] L. A. Ostrovsky, "Nonlinear internal waves in a rotating ocean," Oceanology (Engl. Transl.) **18**, 119 (1978).

[14] B. B. Kadomtsev and V. I. Petviashvili, "On the stability of solitary waves in weakly dispersing media," Sov. Phys. Dokl. **15**, 539 (1970).

[15] P. G. Baines, "The effects of rotation on disturbances upstream of cold fronts approaching Southeast Australia," in *Report on the 2nd International Conference on Southern Hemisphere Meteorology, Wellington, New Zealand* (1986), p. 77.

[16] V. I. Shrira, "On long strongly nonlinear waves in a rotating ocean," Izv., Acad. Sci., USSR, Atmos. Oceanic Phys. **22**, 298 (1986).

[17] R. H. J. Grimshaw, L. A. Ostrovsky, V. I. Shrira, and Y. A. Stepanyants, "Long nonlinear surface and internal gravity waves in a rotating ocean," Surv. Geophys. **19**, 289 (1998).

[18] X. F. Li, C. M. Dong, P. Clemente-Colon, W. G. Pichel, and K. S. Friedman, "Synthetic aperture radar observation of the sea surface imprints of up-stream atmospheric solitons generated by flow impeded by an island," J. Geophys. Res. **209**, 10.1029.2003JC002168 (2004).

[19] E. R. Johnson and G. G. Vilenski, "Flow patterns and drag in near-critical flow over isolated orography," J. Atmos. Sci. **61**, 2909 (2004).

[20] R. Plougonven and V. Zeitlin, "On periodic inertia-gravity waves of finite amplitude propagating without change of form at sharp-density gradient interfaces in the rotating fluid," Phys. Lett. A **314**, 140 (2003).

[21] D. D. Houghton, "Effect of rotation on the formation of hydraulic jumps," J. Geophys. Res. **74**, 1351 (1969).

[22] G. A. Lawrence, "Steady flow over an obstacle," J. Hydraul. Eng. **113**, 981 (1987).

[23] G. F. Lane-Serff, "Topographic and boundary effects on steady and unsteady flow through straits," Deep-Sea Res., Part II **51**, 321 (2004).

[24] R. R. Long, "Some respects of the flow of stratified fluids. II. Experiments with a two-layer system," Tellus **6**, 97 (1954).

[25] R. R. Long, "Blocking effects in flow over obstacles," Tellus **22**, 471 (1970).

[26] D. D. Houghton and A. Kasahara, "Nonlinear shallow fluid flow over an isolated ridge," Commun. Pure Appl. Math. **21**, 1 (1968).

[27] P. G. Baines and P. A. Davies, *Laboratory Studies of Topographic Effects in Rotating and/or Stratified Fluids* (World Meteorological Organization GARP, Geneva, 1980), Chap. 8, p. 233.

[28] P. G. Baines and J. A. Whitehead, "On multiple states in single-layer flows," Phys. Fluids **15**, 298 (2003).

[29] L. J. Pratt, "A note on nonlinear flow over obstacles," Geophys. Astrophys. Fluid Dyn. **24**, 63 (1983).

[30] R. J. LeVeque, *Finite Volume Methods for Hyperbolic Problems* (Cambridge University Press, Cambridge, 2002).

[31] R. J. LeVeque, "Balancing source terms and flux gradients in high resolution Gudonov methods: The quasi-steady wave propagation algorithm," J. Comput. Phys. **146**, 346 (1998).

[32] E. Audusse, F. Bouchut, M.-O. Bristeau, R. Klein, and B. Perthame, "A fast and stable well-balanced scheme with hydrostatic reconstruction for shallow water flows," SIAM J. Sci. Comput. (USA) **25**, 2050 (2004).